

RESEARCH ARTICLE

10.1002/2014JB011122

Key Points:

- Geodetic measurements reveal continued surface deformation following the 2005 Kashmir earthquake
- The data suggest that the surface deformation is primarily due to afterslip
- Contributions from viscoelastic and poroelastic relaxations are negligible

Supporting Information:

- Readme
- Figures S1 and S2

Correspondence to:

K. Wang,
kaw015@ucsd.edu

Citation:

Wang, K., and Y. Fialko (2014), Space geodetic observations and models of postseismic deformation due to the 2005 M7.6 Kashmir (Pakistan) earthquake, *J. Geophys. Res. Solid Earth*, 119, 7306–7318, doi:10.1002/2014JB011122.

Received 13 MAR 2014

Accepted 20 AUG 2014

Accepted article online 26 AUG 2014

Published online 22 SEP 2014

Space geodetic observations and models of postseismic deformation due to the 2005 M7.6 Kashmir (Pakistan) earthquake

Kang Wang¹ and Yuri Fialko¹

¹Institute of Geophysics and Planetary Physics, Scripps Institution of Oceanography, University of California, San Diego, La Jolla, California, USA

Abstract We use the L-band Advanced Land Observing Satellite (ALOS) and C-band Envisat interferometric synthetic aperture data and campaign GPS observations to study the postseismic deformation due to the 2005 magnitude 7.6 Kashmir (Pakistan) earthquake that occurred in the northwestern Himalaya. Envisat data are available from both the descending and ascending orbits and span a time period of ~4.5 years immediately following the earthquake (2005–2010), with nearly monthly acquisitions. However, the Envisat data are highly decorrelated due to high topography and snow cover. ALOS data are available from the ascending orbit and span a time period of ~2.5 years between 2007 and 2009, over which they remain reasonably well correlated. We derive the mean line-of-sight (LOS) postseismic velocity maps in the epicentral area of the Kashmir earthquake using persistent scatterer method for Envisat data and selective stacking for ALOS data. LOS velocities from all data sets indicate an uplift (decrease in radar range), primarily in the hanging wall of the earthquake rupture over the entire period of synthetic aperture radar observations (2005–2010). Models of poroelastic relaxation predict uplift of both the footwall and the hanging wall, while models of viscoelastic relaxation below the brittle-ductile transition predict subsidence (increase in radar range) in both the footwall and the hanging wall. Therefore, the observed pattern of surface velocities indicates that the early several years of postseismic deformation were dominated by afterslip on the fault plane, possibly with a minor contribution from poroelastic rebound. Kinematic inversions of interferometric synthetic aperture radar and GPS data confirm that the observed deformation is consistent with afterslip, primarily downdip of the seismic asperity. To place constraints on the effective viscosity of the ductile substrate in the study area, we subtract the surface deformation predicted by stress-driven afterslip model from the mean LOS velocities and compare the residuals to models of viscoelastic relaxation for a range of assumed viscosities. We show that in order to prevent surface subsidence, the effective viscosity has to be greater than 10^{19} Pa s.

1. Introduction

The M_w 7.6 Kashmir earthquake occurred on 8 October 2005 in the northwestern Himalaya. This area represents a tectonic boundary resulted from the India-Eurasia collision and is characterized by significant seismicity [e.g., Bilham, 2001]. The 2005 Kashmir earthquake is the latest and largest seismic event to date that occurred along the Himalaya arc since the advent of modern space geodesy. The coseismic deformation due to this earthquake has been studied extensively using both geodetic [Avouac et al., 2006; Pathier et al., 2006; Yan et al., 2013] and seismic [Avouac et al., 2006; Parsons et al., 2006] observations. Although there are some variations among the proposed rupture models in terms of rupture geometry and slip distribution, all models suggest that the 2005 Kashmir earthquake ruptured a ~70 km long NE dipping fault with primarily thrust mechanism, with minor component of right-lateral slip, consistent with seismic moment tensor solution determined from modeling of long-period surface waves.

In this study, we investigate surface deformation over several years following the earthquake. Spatiotemporal patterns of postseismic deformation may provide valuable information about mechanical properties of the lithosphere [e.g., Pollitz et al., 2000; Fialko, 2004a; Bürgmann and Dresen, 2008]. Several mechanisms are often invoked to explain the observed transients following large earthquakes, including afterslip, viscoelastic relaxation, and poroelastic rebound [e.g., Bürgmann et al., 2002; Fialko, 2004a; Barbot et al., 2008, 2009]. It is often difficult to separate contributions from different mechanisms due to similar patterns of surface motion, especially in case of strike-slip earthquake [e.g., Savage, 1990; Barbot et al., 2009]. Dip-slip earthquakes, on the

other hand, may give rise to distinct pattern of surface displacements that can be readily identified in the geodetic data [e.g., *Nishimura and Thatcher, 2003; Yu et al., 2003*].

Unfortunately, only limited ground-based observations of postseismic deformation due to the 2005 Kashmir earthquake are available because of the difficult access and mountainous terrain in the epicentral area. Based on data from a campaign-mode GPS survey of 18 sites, *Jouanne et al.* [2011] estimated the temporal-spatial evolution of postseismic deformation. They argued that the GPS data are consistent with afterslip along a flat décollement beneath the main rupture. Most of the GPS measurements with high signal-to-noise ratio were made within ~50 km from the rupture during the first 2 years (2005–2007) after the earthquake. In this study, we complement the available GPS data with C-band Envisat and L-band Advanced Land Observing Satellite (ALOS) synthetic aperture radar (SAR) observations spanning 2005–2010 and 2007–2009, respectively, to characterize the surface deformation over a longer time period and at higher spatial resolution. We compare the observed surface deformation to predictions of models assuming afterslip, viscoelastic relaxation, and poroelastic rebound to place constraints on the effective mechanical properties of lithosphere in the collision zone between the Indian and Eurasian plates.

2. Data

2.1. Envisat

The C-band Envisat data used in this study are from the ascending track T499 (average incidence angle of 41°) and of descending track T463 (average incident angle of 23°). Because of the rugged topography and precipitation in the epicentral area, interferograms suffer from severe decorrelation. To mitigate the problem of geometric and temporal decorrelation, we analyzed the Envisat data using persistent scatter (PS) interferometric synthetic aperture radar (InSAR) technique [e.g., *Ferretti et al., 2000; Hooper et al., 2004, 2007*]. There are 30 scenes available for the ascending track T499, with the first acquisition on 24 October 2005 (about 2 weeks after the earthquake) and last acquisition on 31 May 2010. The descending track T463 has 17 scenes, with first acquisition on 22 October 2005 and last acquisition on 13 June 2009. Figure S1 shows the baseline plots for the respective tracks. We processed the data using StaMPS v3.2 [*Hooper et al., 2009*]. Default parameters (e.g., 800 m cutoff wavelength for low-pass filtering in the space domain and 2 years time window for phase smoothing in the time domain) were used unless noted otherwise. The resulting average line-of-sight (LOS) velocities for the respective tracks T499 and T463 are shown in Figures 2a and 2b, with positive LOS displacements corresponding to surface movement toward the satellite. Data from both tracks yield comparable rate (~cm/yr) of LOS surface movement toward the satellite, primarily on the hanging wall side of the fault. We note that depending on the choice of processing parameters, for example, selection of the master scene, noise threshold, averaging window in the spatial domain, etc., the magnitude of the average LOS velocity can vary by a factor of 2 to 3. For instance, changing the value of a parameter for smoothing the spatially correlated noise in temporal domain, from a default value of 2 years to 0.5 year, increases the LOS velocity in the hanging wall to ~25 mm/yr (cf. Figure 2b). Using a shorter time window for smoothing might be desirable to better characterize the time dependence of postseismic relaxation; however, the resulting LOS velocity is much noisier in the space domain. Also, we found that the deformation accumulated during the first 2 years after the earthquake (2005–2007) is smaller than that accumulated during a later period (2007–2010). This may be due to the residual atmospheric artifacts or some other noise. We thus chose to use a default time window (2 years) for the temporal noise filtering to better characterize the average LOS velocity and the spatial pattern of surface deformation. The radar phase from all unwrapped interferograms was then added and divided by the cumulative time span of the respective interferograms to yield the average LOS velocity during the period of Envisat observations (2005–2010 for ascending track T499 and 2005–2009 for descending track T463).

2.2. ALOS

The L-band ALOS data used in this study are from three frames (F660, F670, and F680) of the ascending track T530 (average incidence angle of ~39°), covering the entire rupture (Figure 1). There are 18 acquisitions over a time period from 2007 to 2011 (see Figure S1 for the baseline plot). We processed the raw SAR data using GMTSAR software [*Sandwell et al., 2011*]. All interferometric pairs satisfy the following criteria: (1) perpendicular baselines less than 700 m, (2) time intervals greater than 1 year, and (3) low root-mean-square (RMS) of interferograms after subtracting the mean radar phase. These criteria are met for a subset of five interferograms with the earliest scene acquired on 17 February 2007 and last scene acquired on 25 August 2009. Because the ALOS data used in our

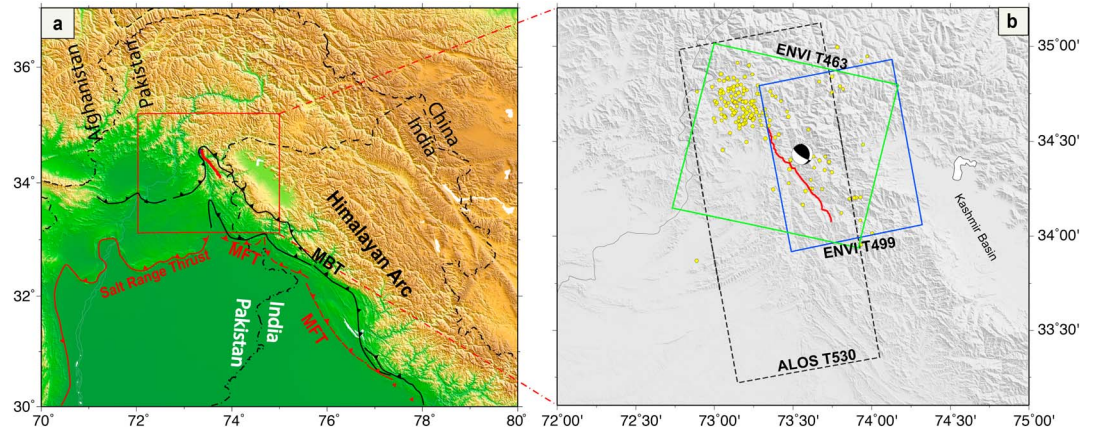


Figure 1. Location of the 8 October 2005 M_w 7.6 Kashmir earthquake. (a) Tectonic settings of the western Himalaya. Major active faults in red are from *Avouac et al.* [2006]. MFT = main frontal thrust; MBT = main boundary thrust (mostly inactive at present). (b) Location of the main shock (beach ball) and $M > 4.5$ aftershocks. Red line denotes the surface trace of coseismic rupture derived from pixel tracking of optical images [Avouac et al., 2006]. Solid and dashed line boxes show the scene coverage of Envisat (blue for ascending track 499 and green for descending track 463) and ALOS (ascending track 530), respectively.

study were in both ALOS User Interface Gateway (AUIG) and Earth Remote Sensing Data Analysis Center (ERSDAC) formats, we processed the interferograms frame by frame and concatenated the unwrapped radar phase ensuring that there are no discontinuities in the overlapping areas. A linear trend was then removed from each interferogram to reduce possible orbital or ionospheric errors. Similar to processing of Envisat data, the radar phase from all five interferograms was added and divided by the cumulative time span of the respective interferograms to produce the average LOS velocity during the period of ALOS observations (2007–2009).

Figure 2c shows the resulting average LOS velocity derived from ALOS data. The pattern of the LOS velocity is similar to that derived from Envisat data, with mainly decreases in radar range on the hanging wall side of the fault. The maximum LOS velocity is up to ~ 2 cm/yr. Compared to the results of Envisat data from persistent scatter (PS) analysis of Envisat data, the LOS velocities of ALOS are noisier, as expected given a smaller set of independent interferograms, but provide a continuous LOS velocity field. We have verified that the inferred uplift pattern is not due to a residual atmospheric noise by inspecting correlation between topography and LOS velocity over the rest of the image. Away from the rupture area, the dependence of the LOS velocity on elevation, if anything, is an increase in the radar range with elevation; thus, positive LOS velocities in the hanging wall would be enhanced if one removes a linear trend inferred from the regression analysis of the LOS velocity and topography in the far field. A linear north-south trending feature that extends ~ 50 km to the south from the middle of the 2005 Kashmir rupture is correlated with the Jhelum fault

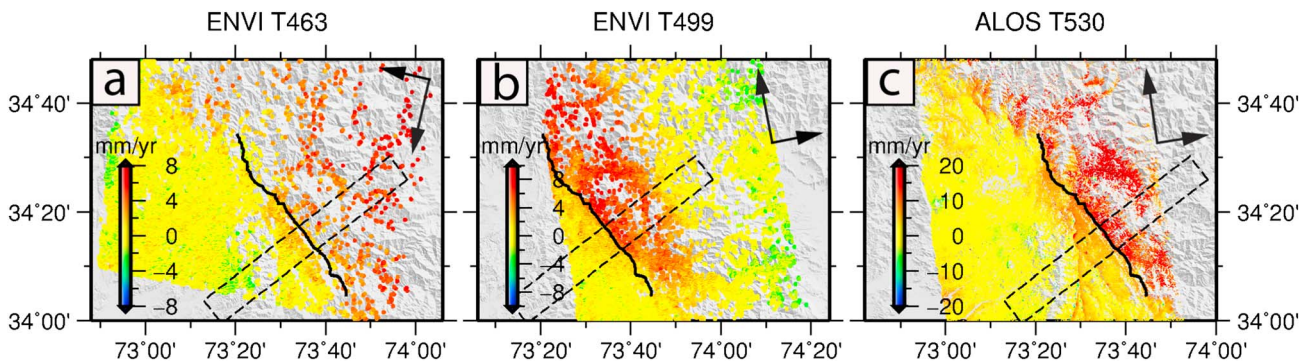


Figure 2. Mean line-of-sight (LOS) velocity maps from permanent scatter (PS) InSAR analysis of (a and b) Envisat data and selective stacking of (c) ALOS interferograms. Positive LOS change corresponds to the surface movement toward the satellite (uplift if all deformation is vertical). Black arrows represent the satellite heading and radar look directions. Dashed black box denotes a profile shown in Figure 3. Note that the magnitude of LOS velocity inferred from PS InSAR analysis of Envisat data is somewhat uncertain, depending on the selection of processing parameters (see the main text for details).

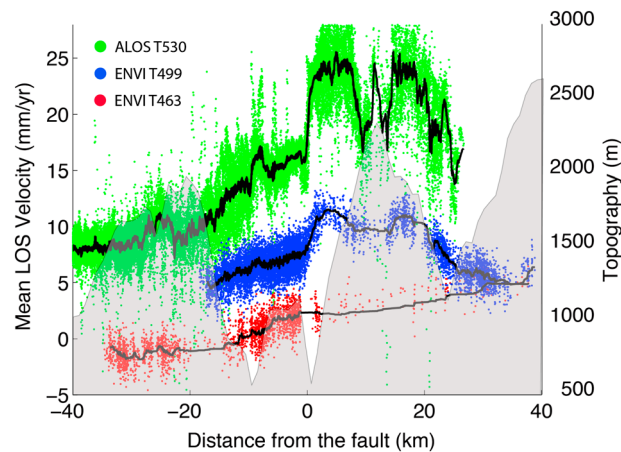


Figure 3. LOS velocities from different satellite tracks (colored circles) and topography (gray shading) along the profile shown by the dashed black line in Figure 2. The LOS velocity profiles have been shifted vertically for better visualization.

described by *Tapponnier et al.* [2006], although it is not clear whether this might represent triggered fault slip or elevation-dependent atmospheric artifacts.

Figure 3 shows the LOS velocities from different satellite tracks along a profile perpendicular to the earthquake rupture. Data from both ALOS track T530 and Envisat ascending track T499 suggest a relatively sharp discontinuity in surface displacements across the fault. The across-fault variations in the LOS velocity are less apparent in the profile from the Envisat descending track T463, possibly due to a destructive interference of the vertical and horizontal displacements along the radar line of sight (Figure 2a). Also, we note that the LOS velocities from the descending Envisat track 463 may

be subject to greater uncertainties due to a fewer acquisitions compared to the ascending track 499 (Figure 2b). The standard deviation of the mean LOS velocity is ~ 3 mm/yr for the Envisat data. For the ALOS data, the uncertainty is more difficult to quantify due to a relatively small number of interferograms used for stacking, but it should be comparable to that of the Envisat data based on the scatter of individual data points from the mean (Figure 3).

As the same general pattern of LOS velocity is seen in all satellite tracks with different look geometries and time periods, the signals shown in Figure 2 are indicative of surface displacements. Interseismic crustal shortening across the Balakot-Bagh thrust (the main rupture of the 2005 M_w 7.6 Kashmir earthquake) is estimated to be slow, at a rate of 1.1–4.1 mm/yr [*Kaneda et al.*, 2008], and has a negligible contribution to the LOS velocities shown in Figure 2. The latter therefore most likely represents postseismic deformation due to the 2005 Kashmir earthquake. In the next section, we will quantitatively analyze the surface displacement fields due to various mechanisms (viscoelastic relaxation, poroelastic rebound, and afterslip) and compare them to the observations to explore what mechanism (or a combination of mechanisms) may have contributed to postseismic deformation following the 2005 Kashmir earthquake.

3. Modeling of Postseismic Deformation

3.1. Viscoelastic Relaxation

We estimate viscoelastic response due to the Kashmir earthquake using a finite element model. As little is known about the lithospheric structure in the Kashmir region, we assume a simple structure consisting of a 20 km thick elastic layer and viscoelastic substrate with linear Maxwell rheology. More complicated models accounting for nonlinear depth-dependent [e.g., *Freed et al.*, 2010; *Takeuchi and Fialko*, 2013] and spatially heterogeneous [e.g., *Rousset et al.*, 2012] rheologies are not warranted given the limited data resolution. The simulations were performed using the finite element code ABAQUS (www.simulia.com/products/abaqus_fea.html). The dimension of the model is 800 km \times 600 km \times 150 km in strike-parallel, strike-perpendicular, and vertical directions, respectively. Zero-displacement boundary conditions are applied at all sides of the model except the top side which is assumed to be stress free. To better resolve the displacement and stress fields close to the fault, the size of the elements gradually increases away from the earthquake rupture. The model contains 1,226,468 tetrahedron elements with near-fault elements as small as ~ 0.5 km.

Several coseismic slip models are available for the 2005 Kashmir earthquake from inversions of geodetic and seismic data. We use two published finite fault models: *Avouac et al.* [2006] hereafter referred to as “model A,” and *Yan et al.* [2013], hereafter referred to as “model Y.” Slip distribution is imposed using a split node technique similar to that used by *Masterlark* [2003]. To directly compare the model predictions to the InSAR-observed surface velocities (Figure 2), we compute the predicted average surface velocity by

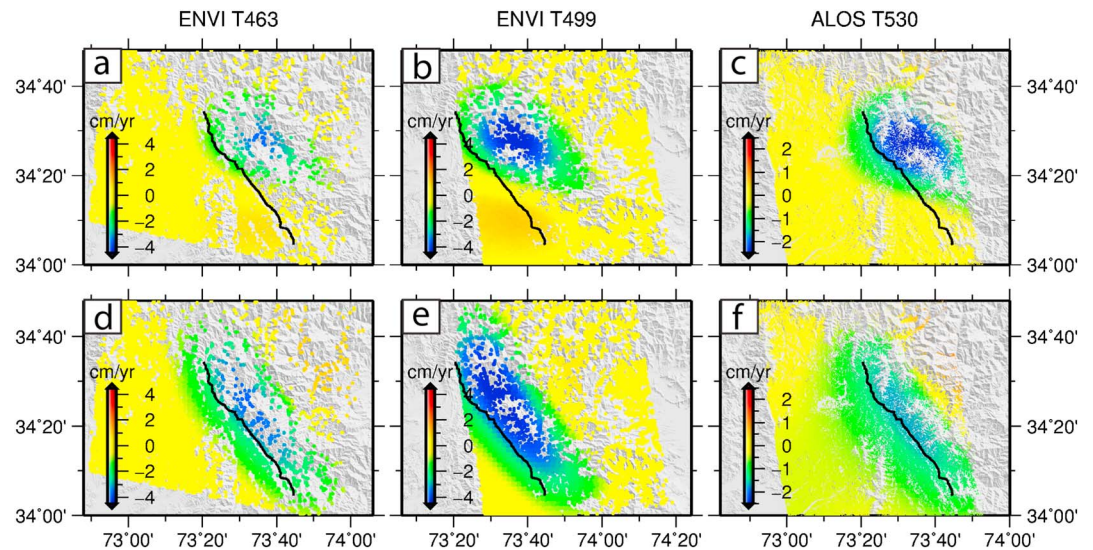


Figure 4. Predicted surface deformation velocity due to the viscoelastic relaxation in the lower crust and upper mantle with effective viscosity of 10^{19} Pa s. The predicted LOS velocity map is obtained by stacking the differential displacements using the intervals corresponding to the SAR interferograms. The sign convention for LOS velocities (positive for decreases in radar range and negative for increases in radar range) is the same as in Figure 2. (a–c) Based upon the coseismic slip model of Avouac *et al.* [2006]. (d–f) Based upon the coseismic slip model of Yan *et al.* [2013].

summing up the differences in surface displacements between the time intervals corresponding to the SAR acquisition dates and divide by the sum of the respective time intervals. The resulting surface velocity is then projected onto the line of sight (LOS) of the satellite to yield the predicted average LOS velocity. Figure 4 (Figures 4a–4c are based on model A, and Figures 4d–4f are based on model Y) shows the predicted average LOS velocities due to viscoelastic relaxation assuming the effective viscosity of the substrate of 10^{19} Pa s. For both Envisat and ALOS tracks, the viscoelastic relaxation models predict increases in radar range that vary continuously across the fault, in contrast to the observed range changes (Figure 2). For the effective viscosity of 10^{19} Pa s, the model predicts increase in radar range at a rate of ~ 4 cm/yr during the Envisat observation period (2005–2010); the rate decreases to ~ 3 cm/yr during the ALOS observation period (2007–2009). The surface velocity fields predicted for the coseismic model Y appear to be more symmetric with respect to the fault and more uniformly distributed along the fault strike from north to the south, compared to the velocities corresponding to model A. These differences are primarily due to the steeper dip angle and more broadly distributed slip in model Y. Changing the viscosity of the substrate affects the average velocity but does not change the overall pattern of surface motion. To examine the sensitivity of LOS velocity to the thickness of viscoelastic layer, we performed a simulation assuming a 20 km thick elastic crust, a 40 km thick lower crust with viscosity of 10^{19} Pa s, and elastic mantle. The LOS velocity in this case is slightly lower and of shorter wavelength, compared to the model shown in Figure 4. We note that the surface subsidence predicted by both models monotonically increases (and decelerates) with time, indicating that the surface deformation field due to viscoelastic relaxation should exhibit a similar pattern during the whole postseismic phase. The significant differences in surface deformation patterns between observations (Figure 2) and models (Figure 4) thus suggest that viscoelastic relaxation was not the dominant mechanism responsible for transient deformation following the 2005 Kashmir earthquake.

3.2. Poroelastic Rebound

We evaluate surface displacements due to poroelastic rebound by differencing the coseismic displacements under undrained and drained conditions. The predicted surface displacements due to poroelastic rebound in the 20 km thick upper crust projected on the line of sight of Envisat and ALOS are shown in Figure 5 (Figures 5a–5c correspond to model A, while Figures 5d–5f correspond to model Y). We use a Poisson's ratio reduction of 0.03 (from undrained value of 0.28 to drained value of 0.25). The poroelastic rebound model based on both coseismic models (models A and Y) shows decreases in the radar range up to ~ 5 cm for both

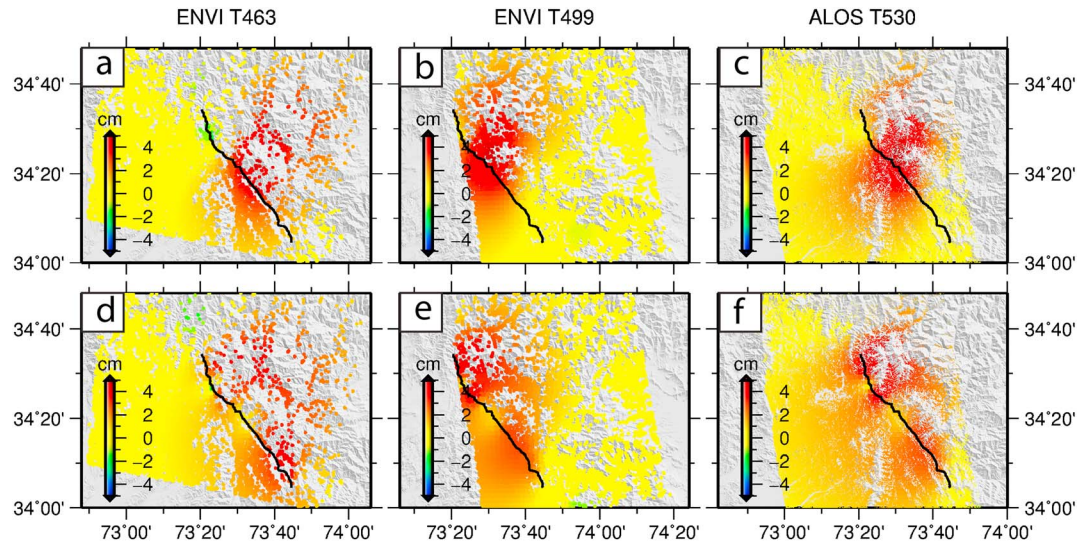


Figure 5. Predicted surface deformation velocity due to the poroelastic rebound in the top 20 km of Earth’s crust, calculated by differencing the coseismic deformation under undrained and drained conditions.

Envisat and ALOS tracks, in a qualitative agreement with the data (Figure 2). However, the poroelastic model predicts a relatively symmetric uplift (decrease in radar range) on both sides of the fault, while the InSAR data suggest that the uplift is primarily concentrated in the hanging wall, although a small amount of uplift may also occur in the footwall (Figures 2 and 3). We note that variations in the reduction of Poisson’s ratio and depth extent of fluid-saturated layer do not alter the surface deformation pattern significantly and only affect the magnitude of surface deformation.

By comparing the InSAR observations (Figure 2) and modeling results (Figures 4 and 5), one can conclude that the viscoelastic and poroelastic responses are not able to explain the InSAR data and alternative mechanisms must be involved.

3.3. Afterslip

The general pattern of postseismic deformation imaged by InSAR data (uplift in the hanging wall and a relatively sharp discontinuity in LOS velocities across the fault; see Figures 2 and 3) is suggestive of a continued slip on the earthquake rupture. To get an insight into the spatial distribution of afterslip on the rupture plane, we performed an inversion using the LOS velocities derived from ALOS and GPS measurements from *Jouanne et al.* [2011]. The fault geometry is based on the coseismic slip model of *Avouac et al.* [2006]. We extended the fault segments both in strike and dip directions. We assumed that the fault has a dip angle of 29° down to depth of 15 km and transitions to a décollement with a dip angle of 10° below 15 km [*Jouanne et al.*, 2011]. The total downdip width of the fault is 60 km. The kinked fault planes were then divided into patches whose sizes gradually increase with depth to ensure a uniform model resolution [*Fialko*, 2004b]. Each individual patch is allowed to have thrust and right-lateral slip components. Laplacian smoothing is applied between adjacent fault patches to avoid abrupt variations in slip. The inversion problem is further regularized by requiring no slip at the fault edges, except the top edge, which is allowed to slip. This leads to a classical minimization problem for the misfit function:

$$F(m, \lambda) = \|Gm - d\| + \lambda \|\nabla^2 m\| \quad (1)$$

where m is the vector of unknown (slip) components, d is the data vector, G is the matrix of Green functions, ∇^2 is the finite different approximation of the Laplacian operator used to smooth the model, and λ is a smoothing factor. We use Green functions for a dislocation in a homogeneous elastic half-space [*Okada*, 1985]. To reduce the computational burden, the average LOS velocity map (Figure 2c) is subsampled using a gradient-based resampling scheme [e.g., *Jónsson et al.*, 2002]. Each resulting data point is then assigned with a weight based on the number of points in the subsampled area [e.g., *Simons et al.*, 2002; *Fialko*, 2004b]. To minimize possible contributions from the postevent seismic activity in the Indus Kohistan Seismic Zone to the northwest of the Kashmir rupture [e.g. *Khawaja et al.*, 2009], data west of 73.3°E longitude were excluded from the inversion.

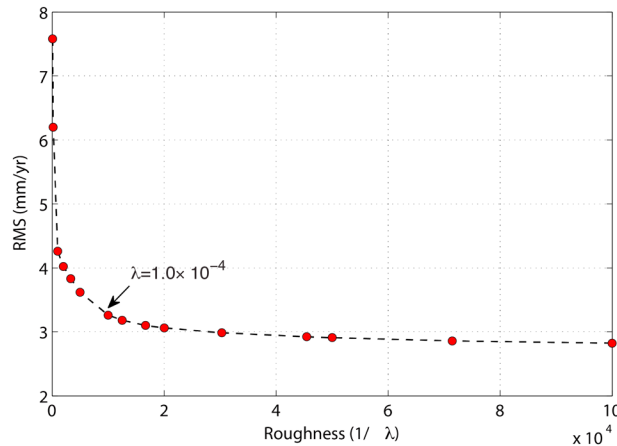


Figure 6. Trade-off curve of the root-mean-square (RMS) of the model misfit with ALOS data versus the roughness of the model.

The optimal value of λ controlling the smoothness of the model was determined using the trade-off relation between the model misfit (residual of model prediction and observation) and the roughness ($1/\lambda$) of the corresponding model (Figure 6). We found that the value of $\lambda = 1.0 \times 10^{-4}$ yields a reasonably smooth slip model with relatively low misfit. The corresponding afterslip model is shown in Figure 8a, along with the coseismic slip distributions of *Avouac et al.* [2006] and *Yan et al.* [2013]. The inferred afterslip mainly occurs down-dip of maximum coseismic slip. The average slip rate during the ALOS observation period (2007–2009) is up

to ~ 80 mm/yr, a factor of ~ 4 lower than the rate estimated from the early (2005–2006) GPS measurements by *Jouanne et al.* [2011].

We next examine whether the GPS measurements of *Jouanne et al.* [2011] are consistent with a model derived from InSAR data. Because most of their campaign-mode GPS measurements were conducted during 2005–2007, it is not straightforward to include them in a joint inversion with the LOS velocity derived from ALOS data that correspond to a later time period (2007–2009). By comparing the time evolution of postseismic displacements and aftershocks, *Jouanne et al.* [2011] suggested that the postseismic displacements can be approximated by the function with log-exponential time dependence [*Fialko, 2004a; Perfettini and Avouac, 2004*].

$$U(t) = A \log(1 + d(\exp(t/t_r) - 1)) \tag{2}$$

where constants $d = 3200$ and $t_r = 8.8$ yr were determined from the analysis of temporal evolution of aftershocks. We performed a grid search to find the best fitting value of A in equation (2) for each GPS site based upon the relative displacements between different occupations available for that site. The displacements for each site were then extrapolated over the time period of ALOS observations and stacked in the same fashion as

ALOS interferograms to yield the average velocity for each GPS site during the ALOS observation period (~ 2007 – 2009). The resulting GPS velocities have azimuths that are similar to the observed ones at the early postseismic epoch but much reduced amplitudes.

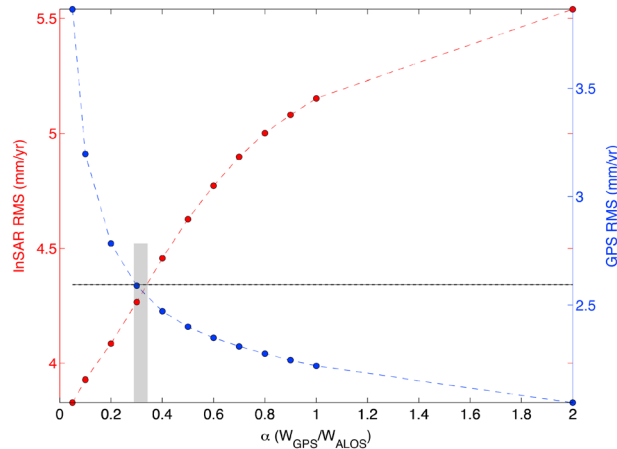


Figure 7. RMS of ALOS and GPS data as a function of their relative weighting. The relative weight of ALOS data is set to be 1, and α is the relative weight of GPS data in the joint inversion. Black dashed line represents 30% increase of the RMS with respect to the minimal value. Shaded area denotes the optimal range of α in which the increases of RMS of both ALOS and GPS data are less than 30%.

We then combined the average LOS velocities from ALOS data with the extrapolated average GPS velocities for the time period of 2007–2009 in a joint inversion for the afterslip distribution. The use of different data sets in the joint inversion requires some choices for relative weighting of the data [e.g., *Simons et al., 2002; Fialko, 2004b*]. The optimal values of the relative weights of these two data sets are determined by examining the trade-off relation between misfit of each data set (ALOS and GPS) and their relative contribution to the inversion. We set the

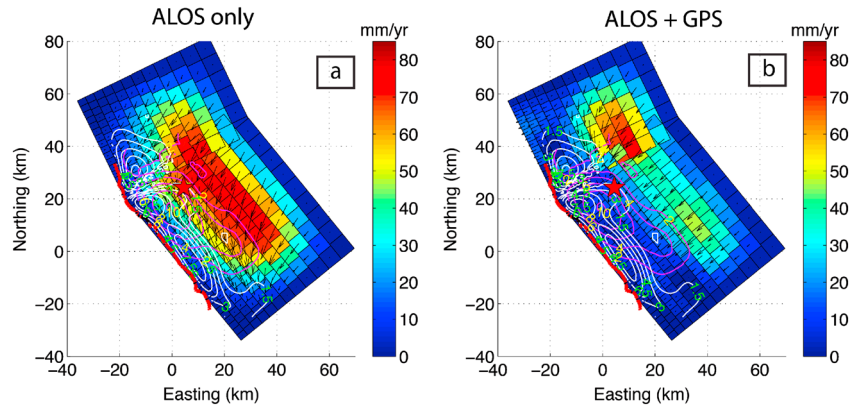


Figure 8. Preferred afterslip models from inversion of (a) ALOS data only and (b) joint inversion of ALOS and GPS data. Magenta lines and white lines represent the contours of coseismic slip distribution from *Avouac et al.* [2006] and *Yan et al.* [2013], respectively. Numbers inside the contours represent slip amplitude in meters. Red star denotes the epicenter of the 2005 Kashmir earthquake. Red line denotes the surface rupture trace derived from pixel-tracking analysis of optical ASTER images [*Avouac et al.*, 2006].

relative weight of ALOS data to be 1 and vary the relative weight of GPS data, α , over a certain range. Figure 7 shows the trade-off between model misfits for each data set (ALOS and GPS) as a function of α . We look for the optimal value of α such that misfits for each data set are within 30% of the respective minimum values. The value of $\alpha = 0.3$ (see the shaded area in Figure 7) was thus chosen as the optimal value for GPS weighting in the joint inversion.

Using the respective optimal values of model smoothness λ and relative weighting α , we infer the afterslip distribution from the joint inversion of ALOS and GPS data (Figure 8b). Similar to the inversion using ALOS data only, the afterslip is mainly concentrated on the periphery of high coseismic slip areas. The maximum slip rate from the joint inversion of ALOS and GPS data is slightly lower than that from inversion of ALOS data only, possibly because the GPS data better constrains the slip rake (the InSAR data from the ascending orbit are only weakly sensitive to strike-slip displacements as the latter are almost orthogonal to the LOS vector). Compared to the afterslip model derived from ALOS data only, the joint inversion has a smaller component of strike slip and a deeper moment centroid of afterslip. Another noticeable difference is the greater amount of afterslip in the northern half of the fault in the joint inversion of ALOS and GPS data. This is consistent with the results of *Jouanne et al.* [2011], who found that afterslip on the Balakot flat (the northern segment) is more pronounced than that on the Bagh flat (the southern segment).

The preferred afterslip model fits both ALOS and GPS data reasonably well. Figure 9 shows the comparison of observed surface deformation and predictions of the afterslip model derived from the ALOS and GPS data

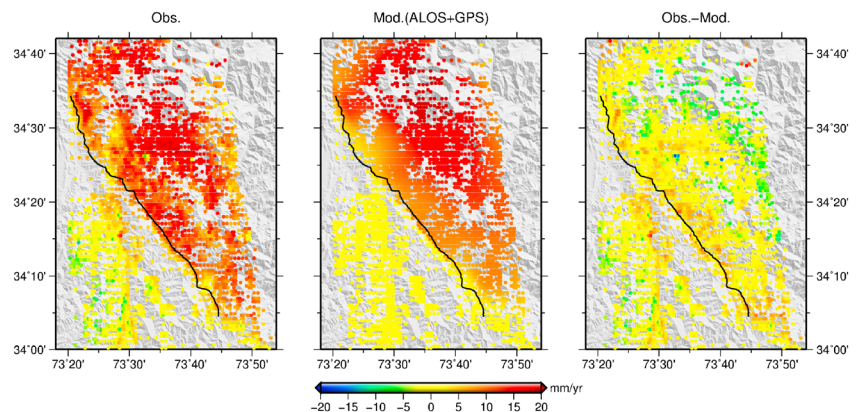


Figure 9. Subsampled mean LOS velocity from ALOS data and prediction of preferred afterslip model (Figure 8b) from joint inversion of ALOS and GPS data.

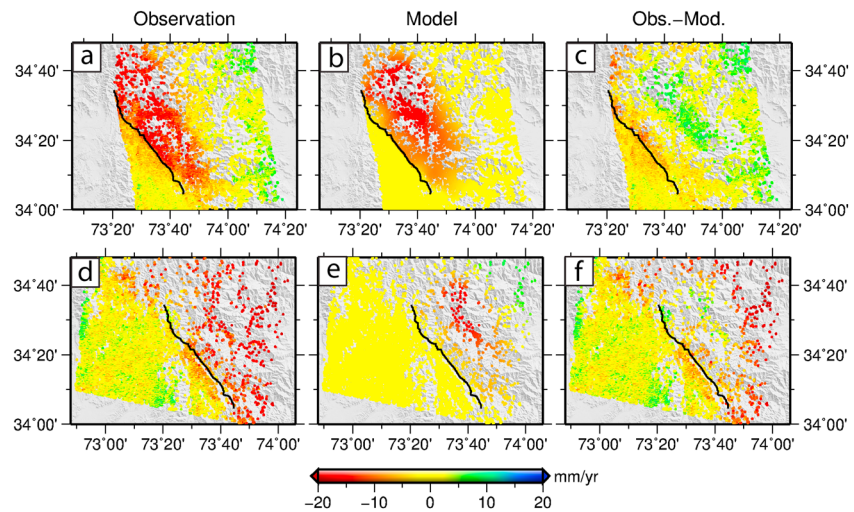


Figure 10. Comparison of surface deformation fields between Envisat observations and afterslip model predictions. (a–c) For the ascending track 499. (d–f) For the descending track 463. Note that the original average LOS velocities have been scaled by a constant (see the text).

(Figure 8b). Overall, the observed uplift on the hanging wall side of the fault has been recovered by the model. Figure 11 shows the comparison of horizontal displacements at the GPS sites of *Jouanne et al.* [2011] (extrapolated and averaged velocities corresponding to the ALOS observation period) and predictions of afterslip, viscoelastic relaxation, and poroelastic rebound models. The overall good agreement between the data and predictions of the afterslip model suggests that deformation during the first several years following the 2005 Kashmir earthquake was dominated by afterslip on the earthquake rupture. The spatial pattern of afterslip appears to have persisted over the period of observations (2005–2010).

We also compared predictions of afterslip model derived from joint inversion of ALOS and GPS data to Envisat observations spanning ~4.5 years immediately after the earthquake. The surface deformation patterns revealed by the Envisat observation are used as an independent check on model predictions. Because of different time periods covered by the data, and substantial (up to a factor of 2 to 3) dependence of the mean LOS velocities on parameters used in the persistent scatter InSAR analysis, we adjust the amplitude of the mean LOS velocity derived from Envisat data to render the best agreement with the afterslip model corresponding to the time period of 2007–2009. Figure 10 shows the comparisons between the adjusted Envisat LOS velocities from the ascending track T499 (Figures 10a–10c) and the descending track T463 (Figures 10d–10f) to the afterslip model predictions. There is a general agreement in the pattern of surface velocities between the Envisat data and the model, suggesting that the early deformation following the 2005 Kashmir earthquake was also dominated by fault afterslip. At some locations close to the rupture trace, the afterslip model seems to underestimate the surface deformation rate (Figures 10c and 11). While this might be in part due to residual errors in the interferograms (e.g., from atmospheric phase delays), another possibility is that these residuals may signify rapidly decaying shallow creep on the earthquake rupture in the first months and years following the earthquake. Similar behavior was documented by continuous GPS measurements elsewhere [e.g., *Burgmann et al.*, 2002; *Barbot et al.*, 2009].

4. Discussion

Rheological properties of the lower crust and upper mantle are of considerable interest, in particular in actively deforming continental settings such as Tibet. Over the past several decades, several end-member models have been proposed to describe the long-term evolution and uplift of the Tibetan Plateau. Some of the proposed models appeal to a highly fluid layer in the lower crust, with viscosity as low as 10^{16} Pa s, that effectively decouples the upper crust from the underlying mantle [e.g., *Royden et al.*, 1997; *Clark and Royden*, 2000]. Such low viscosities are ruled out by studies of postseismic deformation due to large earthquakes in Tibet and adjacent areas, which suggest much higher viscosities of 10^{18} – 10^{19} Pa s [e.g., *Ryder et al.*, 2007, 2011]. In most cases, the published estimates of the effective viscosities are, in fact, lower bounds because of a limited observation period and potential trade-offs between different relaxation mechanisms (i.e., epistemic uncertainties).

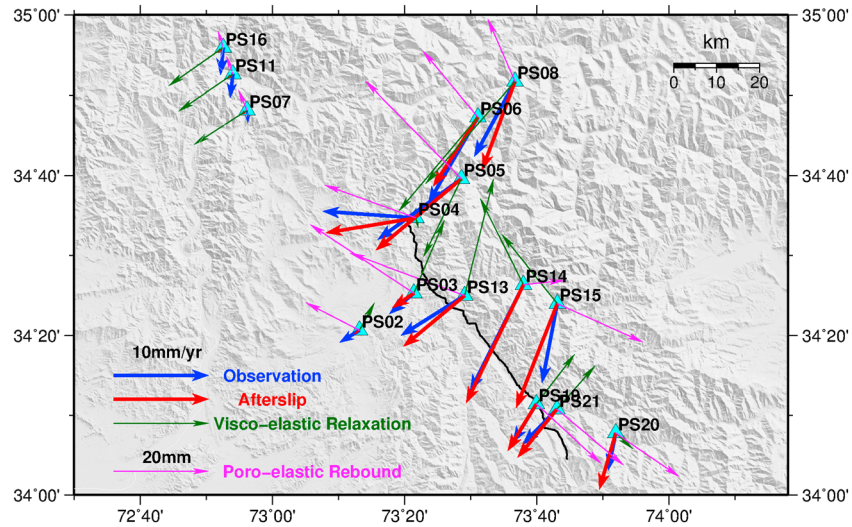


Figure 11. Comparison between the GPS velocities extrapolated over the time of ALOS observation period (2007–2009) and model predictions for various relaxation mechanisms. Surface velocities due to viscoelastic relaxation and displacements due to poroelastic rebound are computed using the coseismic slip model A [Avouac et al., 2006]. Surface velocities due to afterslip are derived from the afterslip model shown in Figure 8b. All the GPS velocities are relative to the station PS01 (not shown in this figure [see Jouanne et al., 2011]).

Our study reveals no obvious contribution of viscoelastic relaxation in the deformation transient following the 2005 Kashmir earthquake. Nevertheless, as the LOS velocities due to viscoelastic relaxation and afterslip have opposite signs on the hanging wall side of the fault, it is possible that the rapid afterslip could overshadow the effects of viscoelastic relaxation (if any). To evaluate how efficiently the signature of viscoelastic relaxation could be canceled by afterslip, we performed an additional set of simulations of stress-driven afterslip assuming that afterslip is governed by the rate-and-state friction [e.g., Dieterich, 1979; Ruina, 1983; Hearn et al., 2002; Barbot et al., 2009]. Simulations were performed using numerical code RELAX [Barbot and Fialko, 2010]. We used the coseismic slip model A [Avouac et al., 2006] to drive afterslip. Afterslip was only allowed in areas that experienced an increase in Coulomb stress (see Barbot et al. [2009] for details). Since little information is available about in situ frictional properties of faults in Kashmir region, we used a velocity-strengthening constitutive law with the effective relaxation time of 10 years. Note that the total amount of afterslip and the respective surface deformation in the limit of full relaxation depend only on the coseismic stress change and the assumed fault geometry and not on the details of the constitutive friction law.

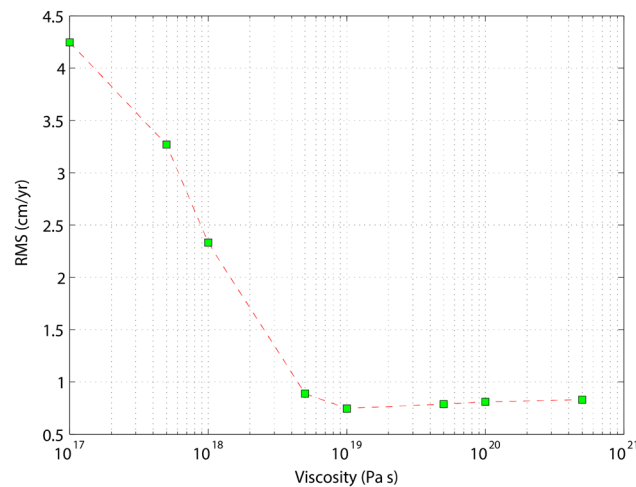


Figure 12. RMS of difference between the viscoelastic model and residual LOS velocities of ALOS data (see the text) as a function of the effective viscosities in the substrate.

The resulting total surface displacement is divided by 10 years and then subtracted from the surface velocity field derived from ALOS data to yield the residual LOS velocities. We compare the residual LOS surface velocities to predictions of viscoelastic relaxation model to test the sensitivity of data to viscosity of the substrate. Figure 12 shows the RMS of difference between the viscoelastic model prediction and the residual LOS velocity as a function of effective viscosity. The misfit is largest for viscosities smaller than 10^{19} Pa s, indicating that it is unlikely that afterslip could be masking a significant

contribution from viscoelastic relaxation. For viscosities above 10^{19} Pa s, because the characteristic relaxation time is greater than the period of observations, the predicted surface deformation is negligible. For the viscosity of 10^{19} Pa s, the predicted rate of surface subsidence (increase in radar range) is ~ 3 cm/yr during the period of ALOS observations. Therefore, 10^{19} Pa s is a conservative lower bound on the effective viscosity of the lower crust of the Western Himalaya region. Future observations may further refine this bound. In particular, a transition from uplift to subsidence may signal an onset of viscoelastic relaxation in the ductile substrate.

Previous studies have suggested that fault slip may induce poroelastic deformation in the host rocks [e.g., *Peltzer et al.*, 1998; *Jónsson et al.*, 2003; *Fialko*, 2004a; *LaBonte et al.*, 2009]. The inferred timescales of poroelastic rebound are on the order of months to years, depending on the hydraulic diffusivity of the host rocks, as well as on the earthquake rupture size [e.g., *Fialko*, 2004a; *Barbot et al.*, 2008; *Barbot and Fialko*, 2010]. For the 2005 Kashmir earthquake, the poroelastic rebound model predicts a uniform uplift (decrease in radar range) on both sides of the fault (Figure 5). The LOS velocities from all three InSAR tracks indicated a significant uplift in the hanging wall and only minor (if any) uplift in the footwall (Figures 2 and 3). The latter could be partly due to the low-pass filtering applied in the data processing. Alternatively, it may be indicative of poroelastic rebound following the Kashmir earthquake. A strong asymmetry in the LOS velocities across the fault (Figures 2 and 3), as well as a poor fit between the poroelastic model and GPS observations (Figure 11), suggests that the contribution of poroelastic rebound to the observed surface deformation following the 2005 Kashmir earthquake is minor, compared to that of afterslip. It remains to be seen whether poroelastic rebound is a common process in the Earth's crust hosting seismogenic faults [*Jónsson et al.*, 2003; *Fialko*, 2004a; *Barbot et al.*, 2008; *Gonzalez-Ortega et al.*, 2014].

The pattern of surface deformation following the 2005 Kashmir earthquake revealed by the Envisat (2005–2010) and ALOS (2007–2009) data is most consistent with afterslip on the earthquake rupture, in agreement with previous studies of early postseismic response due to large dip-slip earthquakes [e.g., *Hsu et al.*, 2002; *Yu et al.*, 2003; *Fialko*, 2009; *Reddy et al.*, 2013; *Copley et al.*, 2012; *Bie et al.*, 2013]. At the same time, vertical motion of the Earth's surface in the epicentral area of several large dip-slip earthquakes might be indicative of viscoelastic relaxation several tens of years after the earthquakes [e.g., *Nishimura and Thatcher*, 2003; *Gourmelen and Amelung*, 2005]. Robust constraints on the effective rheology of the lower crust and upper mantle may require long-term observations that include both the early and late phases of postseismic deformation over a broad range of epicentral distances [e.g., *Takeuchi and Fialko*, 2013]. Space geodetic observations of the early postseismic deformation due to the 2005 Kashmir earthquake indicate that afterslip mainly occurred downdip of the seismogenic asperity. Spatiotemporal distribution of afterslip inferred from kinematic inversions of data spanning different epochs indicates more robust afterslip on the northern section of the fault compared to the southern section, and faster decay of afterslip on the shallow part of the fault, implying heterogeneities in the rate and state frictional properties on the earthquake rupture.

5. Conclusions

We analyzed the C-band Envisat and L-band ALOS interferometric synthetic aperture radar data from the epicentral area of the 2005 M_w 7.6 Kashmir (Pakistan) earthquake that occurred on the northwestern edge of Himalaya. Envisat data are available from both the descending and ascending orbits and span a time period of ~ 4.5 years immediately following the earthquake (2005–2010), with nearly monthly acquisitions. Envisat data are highly decorrelated due to rugged topography and precipitation. ALOS data are available from the ascending orbit and span a time period of ~ 2.5 years between 2007 and 2009, over which they remain reasonably well correlated. The mean line-of-sight postseismic velocity maps in the epicentral area of the Kashmir earthquake are derived using persistent scatterer method for Envisat data and selective stacking for ALOS data. LOS velocities from all data sets indicate an uplift (decrease in radar range), primarily in the hanging wall, of the earthquake rupture (with little uplift in the footwall) over the entire period of SAR observations (2005–2010). Modeling of viscoelastic relaxation in the lower crust and upper mantle predicts subsidence (increase in radar range) in the epicentral area and provides a lower bound on the effective viscosity of the substrate of $\sim 10^{19}$ Pa s. Poroelastic rebound model predicts uplift on both sides of the fault. The available data are best explained by afterslip, possibly with minor contribution from poroelastic rebound. Inversions of InSAR and GPS data suggest that maximum afterslip occurred primarily downdip of the area of maximum coseismic slip and that afterslip on the northern half of the fault was more pronounced compared to that on the southern half of the fault.

Acknowledgments

This work was funded by the National Science Foundation (grant EAR-1321932). We thank two anonymous reviewers and the Associate Editor for comments that improved the manuscript. Original ALOS and Envisat data are copyright by Japanese Aerospace Exploration Agency (JAXA) and European Space Agency (ESA), respectively. The data and computer codes used in this paper are available from the corresponding author.

References

- Avouac, J.-P., F. Ayoub, S. Leprince, O. Konca, and D. V. Helmberger (2006), The 2005, Mw 7.6 Kashmir earthquake: Sub-pixel correlation of ASTER images and seismic waveforms analysis, *Earth Planet. Sci. Lett.*, *249*(3–4), 514–528, doi:10.1016/j.epsl.2006.06.025.
- Barbot, S., and Y. Fialko (2010), A unified continuum representation of post-seismic relaxation mechanisms: Semi-analytic models of afterslip, poroelastic rebound and viscoelastic flow, *Geophys. J. Int.*, *182*(3), 1124–1140, doi:10.1111/j.1365-246X.2010.04678.x.
- Barbot, S., Y. Hamiel, and Y. Fialko (2008), Space geodetic investigation of the coseismic and postseismic deformation due to the 2003 M w 7.2 Altai earthquake: Implications for the local lithospheric rheology, *J. Geophys. Res.*, *113*, B03403, doi:10.1029/2007JB005063.
- Barbot, S., Y. Fialko, and Y. Bock (2009), Postseismic deformation due to the M w 6.0 2004 Parkfield earthquake: Stress-driven creep on a fault with spatially variable rate-and-state friction parameters, *J. Geophys. Res.*, *114*, B07405, doi:10.1029/2008JB005748.
- Bie, L., I. Ryder, S. E. J. Nippress, and R. Burgmann (2013), Coseismic and post-seismic activity associated with the 2008 Mw 6.3 Damxung earthquake, Tibet, constrained by InSAR, *Geophys. J. Int.*, *196*(2), 788–803, doi:10.1093/gji/ggt444.
- Bilham, R. (2001), Earthquakes: Himalayan seismic hazard, *Science*, *293*(5584), 1442–1444, doi:10.1126/science.1062584.
- Bürgmann, R., and G. Dresen (2008), Rheology of the lower crust and upper mantle: Evidence from rock mechanics, geodesy, and field observations, *Annu. Rev. Earth Planet. Sci.*, *36*(1), 531–567, doi:10.1146/annurev.earth.36.031207.124326.
- Burgmann, R., S. Ergintav, P. Segall, E. Hearn, S. McClusky, R. Reilinger, H. Woith, and J. Zschau (2002), Time-dependent distributed afterslip on and deep below the Izmit earthquake rupture, *Bull. Seismol. Soc. Am.*, *92*(1), 126–137, doi:10.1785/0120000833.
- Clark, M., and L. Royden (2000), Topographic ooze: Building the eastern margin of Tibet by lower crustal flow, *Geology*, *28*(8), 703–706, doi:10.1130/0091-7613(2000)28<703.
- Copley, A., J. Hollingsworth, and E. Bergman (2012), Constraints on fault and lithosphere rheology from the coseismic slip and postseismic afterslip of the 2006 M w 7.0 Mozambique earthquake, *J. Geophys. Res.*, *117*, B03404, doi:10.1029/2011JB008580.
- Dieterich, J. H. (1979), Modeling of rock friction: 1. Experimental results and constitutive equations, *J. Geophys. Res.*, *84*(B5), 2161–2168, doi:10.1029/JB084iB05p02161.
- Ferretti, A., C. Prati, and F. Rocca (2000), Nonlinear subsidence rate estimation using permanent scatterers in differential SAR interferometry, *IEEE Trans. Geosci. Remote Sens.*, *38*(5), 2202–2212, doi:10.1109/36.868878.
- Fialko, Y. (2004a), Evidence of fluid-filled upper crust from observations of postseismic deformation due to the 1992 M w 7.3 Landers earthquake, *J. Geophys. Res.*, *109*, B08401, doi:10.1029/2004JB002985.
- Fialko, Y. (2004b), Probing the mechanical properties of seismically active crust with space geodesy: Study of the coseismic deformation due to the 1992 M w 7.3 Landers (southern California) earthquake, *J. Geophys. Res.*, *109*, B03307, doi:10.1029/2003JB002756.
- Fialko, Y. (2009), Study of postseismic deformation due to the 2006 Mw 7.0 Mozambique (East Africa) earthquake using ALOS-PALSAR data, paper presented at 3rd ALOS PI Symposium, Kona, Hawaii, 9–13 Nov.
- Freed, A. M., T. Herring, and R. Bürgmann (2010), Steady-state laboratory flow laws alone fail to explain postseismic observations, *Earth Planet. Sci. Lett.*, *300*(1–2), 1–10, doi:10.1016/j.epsl.2010.10.005.
- Gonzalez-Ortega, A., Y. Fialko, D. Sandwell, A. Nava-Pichardo, J. Fletcher, J. Gonzalez-Garcia, B. Lipovsky, M. Floyd, and G. Funning (2014), El Mayor-Cuapah (Mw 7.2) earthquake: Early near-field postseismic deformation from InSAR and GPS observations, *J. Geophys. Res. Solid Earth*, *119*, 1482–1497, doi:10.1002/2013JB010193.
- Gourmelen, N., and F. Amelung (2005), Postseismic mantle relaxation in the central Nevada seismic belt, *Science*, *310*(5753), 1473–1476, doi:10.1126/science.1119798.
- Hearn, E., R. Bürgmann, and R. Reilinger (2002), Dynamics of Izmit earthquake postseismic deformation and loading of the Düzce earthquake hypocenter, *Bull. Seismol. Soc. Am.*, *92*(1), 172–193, doi:10.1785/0120000832.
- Hooper, A. H., P. S. Zebker, and B. Kampes (2004), A new method for measuring deformation on volcanoes and other natural terrains using InSAR persistent scatterers, *Geophys. Res. Lett.*, *31*, L23611, doi:10.1029/2004GL021737.
- Hooper, A., P. Segall, and H. Zebker (2007), Persistent scatterer interferometric synthetic aperture radar for crustal deformation analysis, with application to Volcán Alcedo, Galápagos, *J. Geophys. Res.*, *112*, B07407, doi:10.1029/2006JB004763.
- Hooper, A., K. Spaans, D. Bekaert, and M. Cuenca (2009), StaMPS/MTI Manual.
- Hsu, Y.-J., N. Bechor, P. Segall, S.-B. Yu, L.-C. Kuo, and M.-F. Kuo (2002), Rapid afterslip following the 1999 Chi-Chi, Taiwan Earthquake, *Geophys. Res. Lett.*, *29*(16), 1754, doi:10.1029/2002GL014967.
- Jónsson, S., H. Zebker, P. Segall, and F. Amelung (2002), Fault slip distribution of the 1999 Mw 7.1 Hector Mine, California, earthquake, estimated from satellite radar and GPS measurements, *Bull. Seismol. Soc. Am.*, *92*(4), 1377–1389, doi:10.1785/0120000922.
- Jónsson, S., P. Segall, R. Pedersen, and G. Björnsson (2003), Post-earthquake ground movements correlated to pore-pressure transients, *Nature*, *424*(July), 179–183, doi:10.1038/nature01758.1.
- Jouanne, F., A. Awan, A. Madji, A. Pêcher, M. Latif, A. Kausar, J. L. Mugnier, I. Khan, and N. A. Khan (2011), Postseismic deformation in Pakistan after the 8 October 2005 earthquake: Evidence of afterslip along a flat north of the Balakot-Bagh thrust, *J. Geophys. Res.*, *116*, B07401, doi:10.1029/2010JB007903.
- Kaneda, H., et al. (2008), Surface rupture of the 2005 Kashmir, Pakistan, earthquake and its active tectonic implications, *Bull. Seismol. Soc. Am.*, *98*(2), 521–557, doi:10.1785/0120070073.
- Khwaja, A. A., R. S. Yeats, A. Hussain, and S. A. Khan (2009), New data on the Indus Kohistan seismic zone and its extension into the Hazara-Kashmir Syntaxis, NW Himalayas of Pakistan, *J. Seismol.*, *13*, 339–361, doi:10.1007/s10950-008-9139-6.
- LaBonte, A., K. Brown, and Y. Fialko (2009), Hydrogeologic detection and finite-element modeling of a slow-slip event in the Costa Rica prism toe, *J. Geophys. Res.*, *114*, B00A02, doi:10.1029/2008JB005806.
- Masterlark, T. (2003), Finite element model predictions of static deformation from dislocation sources in a subduction zone: Sensitivities to homogeneous, isotropic, Poisson-solid, and half-space assumptions, *J. Geophys. Res.*, *108*(B11), 2540, doi:10.1029/2002JB002296.
- Nishimura, T., and W. Thatcher (2003), Rheology of the lithosphere inferred from postseismic uplift following the 1959 Hebgen Lake earthquake, *J. Geophys. Res.*, *108*(B8), 2389, doi:10.1029/2002JB002191.
- Okada, Y. (1985), Surface deformation due to shear and tensile faults in a half-space, *Bull. Seismol. Soc. Am.*, *75*(4), 1135–1154.
- Parsons, T., R. S. Yeats, Y. Yagi, and A. Hussain (2006), Static stress change from the 8 October, 2005 M = 7.6 Kashmir earthquake, *Geophys. Res. Lett.*, *33*, L06304, doi:10.1029/2005GL025429.
- Pathier, E., E. J. Fielding, T. J. Wright, R. Walker, B. E. Parsons, and S. Hensley (2006), Displacement field and slip distribution of the 2005 Kashmir earthquake from SAR imagery, *Geophys. Res. Lett.*, *33*, L20310, doi:10.1029/2006GL027193.
- Peltzer, G., P. Rosen, F. Rogez, and K. Hudnut (1998), Poroelastic rebound along the Landers 1992 earthquake surface rupture, *J. Geophys. Res.*, *103*(B12), 30,131–30,145, doi:10.1029/98JB02302.

- Perfettini, H., and J. Avouac (2004), Postseismic relaxation driven by brittle creep: A possible mechanism to reconcile geodetic measurements and the decay rate of aftershocks, application to the Chi-Chi earthquake, Taiwan, *J. Geophys. Res.*, *109*, B02304, doi:10.1029/2003JB002488.
- Pollitz, F., G. Peltzer, and R. Bürgmann (2000), Mobility of continental mantle: Evidence from postseismic geodetic observations following the 1992 Landers earthquake, *J. Geophys. Res.*, *105*(1999), 8035–8054, doi:10.1029/1999JB900380.
- Reddy, C., P. Sunil, R. Burgmann, D. Chandrasekhar, and T. Kato (2013), Postseismic relaxation due to Bhuj earthquake on January 26, 2001: Possible mechanisms and process, *Nat. Hazards*, *65*, 1119–1134, doi:10.1007/s11069-012-0184-7.
- Roussel, B., S. Barbot, J.-P. Avouac, and Y.-J. Hsu (2012), Postseismic deformation following the 1999 Chi-Chi earthquake, Taiwan: Implication for lower-crust rheology, *J. Geophys. Res.*, *117*, B12405, doi:10.1029/2012JB009571.
- Royden, L. H., B. C. Burchfiel, R. W. King, E. Wang, Z. Chen, F. Shen, and Y. Liu (1997), Surface deformation and lower crustal flow in Eastern Tibet, *Science*, *276*(5313), 788–790, doi:10.1126/science.276.5313.788.
- Ruina, A. (1983), Slip instability and state variable friction laws, *J. Geophys. Res.*, *88*(B12), 10,359–10,370, doi:10.1029/JB088iB12p10359.
- Ryder, I., B. Parsons, T. J. Wright, and G. J. Funning (2007), Post-seismic motion following the 1997 Manyi (Tibet) earthquake: InSAR observations and modelling, *Geophys. J. Int.*, *169*(3), 1009–1027, doi:10.1111/j.1365-246X.2006.03312.x.
- Ryder, I., R. Bürgmann, and F. Pollitz (2011), Lower crustal relaxation beneath the Tibetan Plateau and Qaidam Basin following the 2001 Kokoxili earthquake, *Geophys. J. Int.*, *187*(2), 613–630, doi:10.1111/j.1365-246X.2011.05179.x.
- Sandwell, D., R. Mellors, X. Tong, M. Wei, and P. Wessel (2011), *GMTSAR: An InSAR Processing System Based on Generic Mapping Tools*, *Scripps Inst. Oceanogr. Tech. Rep.*, pp. 14–19, Scripps Institution of Oceanography, UC San Diego.
- Savage, J. (1990), Equivalent strike-slip earthquake cycles in half-space and lithosphere-asthenosphere Earth models, *J. Geophys. Res.*, *95*(B4), 4873–4879, doi:10.1029/JB095iB04p04873.
- Simons, M., Y. Fialko, and L. Rivera (2002), Coseismic deformation from the 1999 Mw 7.1 Hector Mine, California, earthquake as inferred from InSAR and GPS observations, *Bull. Seismol. Soc. Am.*, *92*(4), 1390–1402, doi:10.1785/0120000933.
- Takeuchi, C. S., and Y. Fialko (2013), On the effects of thermally weakened ductile shear zones on postseismic deformation, *J. Geophys. Res. Solid Earth*, *118*, 6295–6310, doi:10.1002/2013JB010215.
- Tapponnier, P., G. King, and L. Bollinger (2006), Active faulting and seismic hazard in the western Himalayan Syntaxis, Pakistan, International Conference on 8th October 2005 Earthquake in Pakistan: Its Implications and Hazard Mitigation, Jan. 18–19, Islamabad, Pakistan, p. 6–7 (Extended Abstract).
- Yan, Y., V. Pinel, E. Trouve, E. Pathier, J. Perrin, P. Bascou, and F. Jouanne (2013), Coseismic displacement field and slip distribution of the 2005 Kashmir earthquake from SAR amplitude image correlation and differential interferometry, *Geophys. J. Int.*, *193*(1), 29–46, doi:10.1093/gji/ggs102.
- Yu, S.-B., Y.-J. Hsu, L.-C. Kuo, H.-Y. Chen, and C.-C. Liu (2003), GPS measurement of postseismic deformation following the 1999 Chi-Chi, Taiwan, earthquake, *J. Geophys. Res.*, *108*(B11), 2520, doi:10.1029/2003JB002396.